New seawater dielectric constant parametrization and application to SMOS retrieved salinity

Jacqueline Boutin, Jean-Luc Vergely, Fabrice Bonjean, Xavier Perrot, Yiwen Zhou, Emmanuel Dinnat, Roger Lang, David Le Vine, Roberto Sabia

HAL Id: hal-04149522
https://hal.science/hal-04149522

Submitted on 13 Nov 2023

New Seawater Dielectric Constant Parametrization and Application to SMOS Retrieved Salinity

Jacqueline Boutin, *Member, IEEE*, Jean-Luc Vergely, Fabrice Bonjean, Xavier Perrot, Yiwen Zhou, *Member, IEEE,* Emmanuel Dinnat, *Senior Member, IEEE,* Roger Lang, *Fellow, IEEE,* David Levine, *Fellow, IEEE*, and Roberto Sabia, *Member IEEE*

Abstract— **The accuracy of the Sea Surface Salinity (SSS) retrieved from L-Band radiometer measurements is strongly dependent on the reliability of the dielectric constant model. Two new parametrizations were recently developed based on one hand on the Soil Moisture and Ocean Salinity (SMOS) satellite multi-angular brightness temperature measurements by Boutin et al. (2021) (BV), and on the other hand on new George Washington University laboratory measurements by Zhou et al. (2021) (GW2020). These two approaches are fully independent. For most SSS and Sea Surface Temperature (SST) conditions commonly observed over the open ocean, the relative variations of brightness temperatures Tb simulated through the BV and GW2020 parametrizations agree particularly well, and better than with earlier parametrizations previously used in the SMOS, Soil Moisture Active Passive (SMAP) and Aquarius SSS retrievals. Nevertheless, uncertainty remains, especially below 10°C where a ~0.1K relative difference between the two models is observed. This motivates the development of a revised parameterization, BVZ, based on a methodology similar to that used to derive BV but using GW2020 instead of SMOS measurements. Compared to the GW2020 parameterization, BVZ is derived with a reduced number of degrees of freedom, it relies on TEOS10 PSS78 conductivity-salinity relationship and on previously derived static permittivity of fresh water. One month per season of SMOS data have been reprocessed in 2018 using BV, GW2020 and BVZ. We find the best overall agreement between SMOS SSS and Argo SSS with BVZ parametrization, with noticeable improvement in the 5°C-15°C SST range.**

Index Terms—**Sea surface salinity, Dielectric constant, L-band microwave radiometry**

I. INTRODUCTION

Remote sensing of Sea Surface Salinity (SSS) is essential for monitoring and understanding the Earth's climate, the Earth's water cycle and the global ocean circulation (see reviews in [1-3]). Salinity is a fingerprint of freshwater input to the ocean (runoff, precipitation, ice melt) and a tracer of water masses. Salinity, together with temperature and pressure, determines the density of seawater (in particular the vertical stratification of the ocean). As such, it governs the thermohaline circulation at high latitudes (in cold waters, density is mainly determined by salinity) and the penetration of freshwater, heat, carbon and biogeochemical tracers exchanged at air-sea, land-sea and ice-sea interfaces into the ocean.

L-band (1.4GHz) radiometry is the technique used since 2010 to measure SSS from space. SSS retrieval is very challenging in terms of radiometric signal modelling due to low signal-to-noise ratio. The radiative transfer models (RTM) are optimized to take into account, in addition to the salinity and temperature impact on the seawater dielectric constant, effects related to wind (sea surface roughness, foam emission), atmospheric emission and absorption, and scattering of galactic noise by the sea surface [2]. The various components of the RTM have in general a theoretical basis, however adjusting their parameterizations to match the radiometric measurements is often necessary. This matching procedure is tricky since isolating each effect from the others is difficult, e.g., most strong winds are observed in cold areas, or singling out any effect from measurement contaminations, such as ice contamination in very cold areas, is a challenge.

Therefore, improving the accuracy of the dielectric constant parametrization using information independent from spaceborne radiometric measurements is crucial. In this sense, laboratory measurements of the seawater dielectric combined

J. Boutin is with the Laboratoire d'Océanographie et du Climat: Expérimentations et Approches Numériques– Institut Pierre Simon Laplace (LOCEAN/IPSL), Sorbonne Université, CNRS, IRD, MNHN, Paris, France (e-mail: jb@locean.ipsl.fr).

J.L. Vergely is with ACRI-st, Guyancourt, France (e-mail: jean-luc.vergely@acri-st.fr).

F. Bonjean is with LOCEAN/IPSL, Sorbonne Université, CNRS, IRD, MNHN, Paris, France (e-mail: fabrice.bonjean@locean.ipsl.fr).

X. Perrot was with LOCEAN/IPSL, Sorbonne Université, CNRS, IRD, MNHN, Paris, France. He is now with LMD/IPSL (xavier.perrot@lmd.ens.fr).

Y. Zhou is with Swiss Federal Institute for Forest, Snow and Landscape Research (WSL), Birmensdorf, Switzerland (email: yiwen.zhou@wsl.ch).

E.D. Dinnat is with NASA Goddard Space Flight Center, Greenbelt, MD 20771, USA (e-mail: emmanuel.dinnat@nasa.gov).

R. Lang is with GWU (lang@gwu.edu).

D. Levine is with NASA Goddard Space Flight Center, Greenbelt, MD 20771, USA (e-mail: david.levine@nasa.gov).

R. Sabia is with Telespazio-UK for ESA, ESRIN, 00044 Frascati, Italy (e-mail: roberto.sabia@esa.int).

with theoretical considerations are extremely valuable to improve the full RTMs and the retrieved SSS.

The present study aims at understanding the origin of the remaining differences between BV and GW2020 parametrizations, at proposing a new parametrization to reconcile both approaches, and at evaluating the performance of this revised parametrization based on SMOS measurements. Dielectric constant models are presented in section II, together with a critical analysis of the assumptions behind each parametrization, the information provided by laboratory measurements, and a revised parametrization. The SMOS salinity retrieval results are shown in section III. Discussion and conclusion are given in section IV.

II. DIELECTRIC CONSTANT MODELS

A. Dielectric constant models at L band: state of the art

A complete historical review and intercomparison of dielectric constant parametrizations in use at L-Band is given in [4]. Until recently, satellite SSS were retrieved using dielectric constant parametrizations from either Klein and Swift (KS, [5]) or Meissner and Wentz (MW, [6, 7]). Recently, two new parametrizations have been derived from laboratory measurements made at the George Washington University (GW2020; [8]) and from SMOS measurements (BV; [9]). Remarkably, the brightness temperatures, Tb, simulated using these two new parameterizations (Tb$_{BV}$ and Tb$_{GW2020}$) show similar patterns of differences when compared with Tb simulated using the KS (Tb$_{KS}$) or MW (Tb$_{MW}$) parameterizations under conditions of SSS and sea surface temperature (SST) commonly encountered in the open ocean. Figure 1a-e shows these differences at nadir. At other incidence angles, the patterns of the differences in the (SST, SSS) plane remain qualitatively similar, the magnitude of the differences generally increases in vertical polarization, V-pol, and decreases in horizontal polarization, H-pol. Statistics of the differences at nadir and at 40°, close to SMAP incidence angle are reported in Table 1. Compared with Tb$_{KS}$, Tb$_{BV}$ and Tb$_{GW2020}$ are higher at high SST and lower at low SST. Between 5 and 20°C, Tb$_{BV}$ and Tb$_{GW2020}$ are lower than Tb$_{MW}$ (Figure 1c-d). However, Tb$_{BV}$ is higher than Tb$_{GW2020}$ by ~0.1K on average over all SSS, SST (Table 1). This systematic difference is possibly related to uncertain absolute calibration of satellite radiometric measurements [4]. The STD of (Tb$_{BV}$-Tb$_{GW2020}$) is the smallest of the ones observed between the Tb simulated with the various relationships (last column of Table 1).

The various sea water dielectric constant parametrizations considered in this paper can be expressed with a single Debye relaxation law [10]:

$$\varepsilon(T,S) = \varepsilon_\infty + \frac{\varepsilon_s - \varepsilon_\infty}{1 + j\omega\tau} - \frac{j\sigma}{\varepsilon_0\omega} \qquad (1)$$

where j is the imaginary unit, ε_∞ is the dielectric constant at very high frequency, ε_s is the static (zero frequency) dielectric constant, τ is the relaxation time in seconds, ω is the angular frequency ($2\pi \cdot 1.4135 \cdot 10^9$ Hz.rad in the case of SMOS), σ is the ionic conductivity of the dissolved salts in sea water in siemens per meter, ε_0 is the permittivity of free space. The differences

between the considered parametrizations come from the varying dependencies of the above parameters on temperature and salinity (T,S).
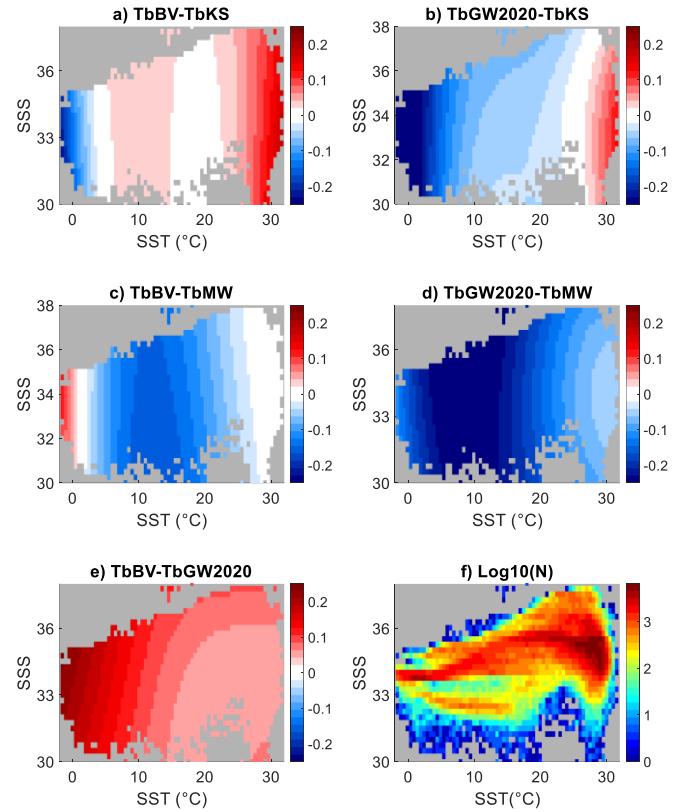

Figure 1: Differences in Tb at nadir (Kelvin) simulated using various dielectric constant models, plotted in the (SST, SSS) plane: a) (Tb$_{BV}$-Tb$_{KS}$); b) (Tb$_{GW2020}$-Tb$_{KS}$); c) (Tb$_{BV}$-Tb$_{MW}$) ; d) (Tb$_{GW2020}$-Tb$_{MW}$), e) (Tb$_{BV}$-Tb$_{GW2020}$), and f) number of sample points. The differences are plotted for SSS and SST commonly observed in the open ocean (70°N-70°S).

TABLE 1
MEAN AND STD DIFFERENCES OF TB (KELVIN) AT NADIR, 40° V-POL AND 40° H-POL, SIMULATED WITH VARIOUS DIELECTRIC CONSTANT MODELS OVER (SSS, SST) PAIRS PLOTTED ON FIGURE 1

	Mean (0°/40V/40H)	Std (0°/40V/40H)
Tb$_{BV}$-Tb$_{KS}$	0.04/0.05/0.03	0.10/0.12/0.08
Tb$_{GW2020}$-Tb$_{KS}$	-0.06/-0.08/-0.05	0.14/0.11/0.12
Tb$_{BV}$-Tb$_{MW}$	-0.06/-0.07/-0.05	0.07/0.08/0.06
Tb$_{GW2020}$-Tb$_{MW}$	-0.16/0.20/0.14	0.07/0.08/0.06
Tb$_{BV}$-Tb$_{GW2020}$	0.10/0.11/0.08	0.06/0.05/0.05

1) BV parametrization

BV parametrization was developed based on the model proposed by [11] (SoTr model in the following). It includes a description of the total polarization of sea water. At L-Band, the model tends to a formulation very close to a single Debye relaxation law, replacing ε_∞ by the intermediate frequency

dielectric constant considered in a double Debye relaxation law, ε_1. The SoTr model is based on several main assumptions which are recalled below. In seawater, ε_s is assumed to decrease as all the water molecules that are in the vicinity of an ion orient themselves with respect to the ion. These water molecules are assumed not to contribute to the orientation polarization of seawater. The number of water molecules that orient themselves about the dissolved ions is assumed to be directly proportional to the number of ions so that ε_s decreases linearly as S increases. The SoTr model also assumes that τ is not affected by the addition of ions, so that τ is independent on S. Hence, under these assumptions, equation (1) can be rewritten as:

$$\varepsilon_{BV}(T,S) = \epsilon_1(T,S=0) + \frac{\epsilon_s(T,S=0)\cdot(1-\boldsymbol{\alpha(T)}\cdot S)-\epsilon_1(T,S=0)}{1+j\omega\tau(T,S=0)} - \frac{j\sigma(T,S)}{\varepsilon_0\omega} \quad (2)$$

where α is independent of S. BV parametrization follows (2) where the bold font is used to indicate that $\alpha(T)$ is a fitted parameter. In (2), all the salinity dependencies are contained in σ and in the term $(1-\alpha(T)\cdot S)$. The SMOS Tb measurements were not enough to fit several independent parameters. Hence, [9] chose to fit only $\alpha(T)$ with SMOS-derived pseudo dielectric constant, and to keep parametrizations derived earlier as in [6] for freshwater quantities (ε_s ; ε_1; τ), and for σ. Parameter α was adjusted to SMOS data, using a degree-3 polynomial (4 fitted parameters) depending on T. However, [9] noticed that, over T,S conditions commonly encountered over open ocean, very similar $\varepsilon(T,S)$ fitted values could have been obtained with a fit of $\tau(T)$ instead of $\alpha(T)$.

2) GW2020 parametrization
GW2020 parametrization [8] was derived from measurements performed in the laboratory of George Washington (GW) University. The laboratory facility was thoroughly designed, and very accurate measurements of the complex dielectric constant of seawater were carried out [12, 13]. Four quantities (ε_s; α; τ; σ) (in bold in equation (3)) involved in the single Debye relaxation law were adjusted to those measurements with the following T, S dependencies:

$$\varepsilon_{GW2020}(T,S) = \varepsilon_\infty + \frac{\boldsymbol{\varepsilon_s(T)}\ (1-\boldsymbol{\alpha(T,S)}\cdot S)-\varepsilon_\infty}{(1+j\omega\boldsymbol{\tau(T)})} - \frac{j\boldsymbol{\sigma(T,S)}}{\varepsilon_0\omega} \quad (3)$$

A total of 21 parameters were fitted, involving dependencies of the four quantities on T (up to the power of 2), S (up to the power of 3) and S·T cross product.

B. Critical analysis of BV and GW2020 parametrizations
BV parametrization was derived from SMOS data. Real (ε') and imaginary (ε'') parts of the dielectric constant cannot be retrieved independently from Tb measurements. Only a pseudo dielectric constant, close to the dielectric constant modulus, can be retrieved from SMOS Tb [14]. Consequently, ε' and ε'' cannot be fully adjusted using SMOS data only, unlike the adjustment performed with laboratory measurements. Moreover, the SMOS adjustment is performed only over open ocean conditions, with most S values above 31pss (Figure 1f), and with relatively fewer and uncertain values in cold waters, due to possible ice contamination. When BV parametrization

was applied to SSS retrieval from updated SMOS level 1 Tb and from Aquarius Tb, slight positive biases (≤0.2 pss) remained with respect to Argo SSS for SST lower than 7°C (Fig. 7 and 8 in [1]). Given uncertainties in the roughness correction in the Southern Ocean and uncertainties associated with ice-sea transition effects on the Tbs, it was not possible to draw firm conclusion. Lastly, part of SMOS and Aquarius Tb calibrations use some information coming from RTM entailing that the absolute value of Tb is subject to uncertainty.
GW laboratory ε measurements have been performed for 80 pairs of temperatures and salinities. The measurements were conducted for salinities ranging between 0 and 38pss with a better sampling at high SSS, under temperatures ranging between -1.5°C and 35°C with a better sampling at low temperatures [8]. Comparisons between Tb simulated using BV (Tb_{BV}) and Tb derived from GW laboratory measurements (Tb_{GWlab}) (Figure 2a) reveal the following issues:
- Above 30 pss, TbBV is mostly above TbGWlab. For S between 33pss and 36pss, corresponding to the most commonly observed SSS in the open ocean (Figure 1f), this bias amounts to 0.15K (Table 2). It is relatively independent of S. It is attributable to the uncertainty in SMOS absolute calibration over open ocean (T,S) conditions. In practice, it does not strongly affect SMOS retrieved SSS because SMOS Tb are first corrected for their mean difference with respect to the modelled Tb over the south east Pacific region (the so-called Ocean Target Transformation, OTT, procedure).
- Below 20 pss, the difference between Tb_{BV} and Tb_{GWlab} appears to be independent of T whereas at higher S, it increases as T decreases.
- As expected by construction, differences between Tb simulated with GW2020, Tb_{GW2020}, and Tb_{GWlab} (Figure 2b) are much smaller, with a mean difference near 0.00K instead of 0.09K with (Tb_{BV} -Tb_{GWlab}) and a STDD of 0.09K instead of 0.11K.
Comparisons between ε estimated with BV (ε_{BV}), GW2020 (ε_{GW2020}), or measured in laboratory (ε''_{GWlab}) (Figure 2) show that ε''_{BV} - ε''_{GWlab} are almost as close as ε''_{GW2020} - ε''_{GWlab} (Figure 2d,f). Meanwhile, differences between ε'_{BV} and ε'_{GWlab} (Figure 2c) become more negative with increasing S. They partly reflect, in the opposite sense, differences between Tb_{BV}-Tb_{GWlab} (Figure 2a), which underlines that the main weakness of BV dielectric constant comes from its real part.
GW2020 parametrization was derived from GW laboratory measurements. These were performed with T ranging from -1.5°C to 35°C and S from 0 to 38pss. While these T,S conditions are more representative of the open ocean conditions than the laboratory measurements carried out previously (for instance KS parametrization was derived only from measurements taken at temperatures above 5°C), the number of different (T,S) conditions is limited to 80. This imposes a theoretical constraint on the number of degrees of freedom to be considered when deriving a new parametrization, but GW2020 did not consider this. The more free parameters a model has, the better the model fits to the data. Thus, when seeking to minimize the residuals to the measurements, one generally manages to reduce the residuals by increasing the number of coefficients. However, adding too many coefficients

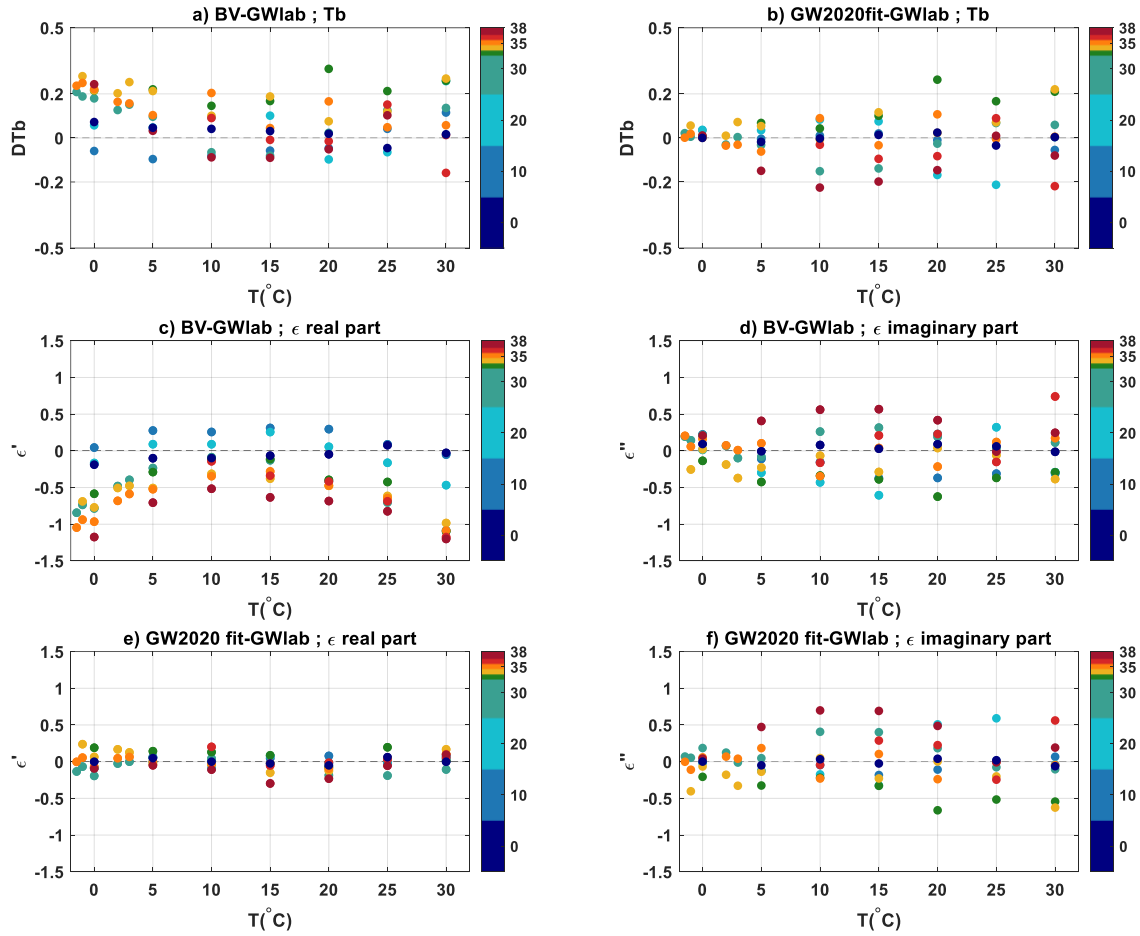may lead to overfitting and, thus, be less conducive to generalization.

Figure 2: a, b) Difference in Tb at nadir (a) between Tb$_{BV}$ and Tb$_{GWlab}$ and (b) between Tb$_{GW2020}$ and Tb$_{GWlab}$. All plots are functions of T (x axis) and S (color scale). c, d) Difference between ε$_{BV}$ and ε$_{GWlab}$: c) real part and d) imaginary part. e, f) Difference between ε$_{GW2020}$ and ε$_{GWlab}$: e) real part and f) imaginary part. For each plot, mean difference and standard deviation of difference are reported in Table 2.

A second limitation of GW2020 parametrization comes from the conductivity fit. Seawater samples used in the GW laboratory experiments were purchased from Ocean Scientific International Limited (OSIL), Havant, U.K., and have a salinity calibrated using the PSS-78 conductivity-salinity relationship. Hence, to remain consistent with the reference salinity used in the GW laboratory experiments, one has to use the PSS-78 conductivity salinity relationship. The PSS-78 conductivity [15] is almost the same as [16] conductivity salinity relationship used in MW, the difference remaining always less than 1.10^{-3} S m^{-1} (with a maximum observed at high S and high T), that is an order of magnitude less than the difference between GW2020 conductivity and MW conductivity (Fig 9 in [8]).

TABLE 2
MEAN AND STD DIFFERENCES OF TB AT NADIR AND ε DERIVED FROM DIELECTRIC CONSTANT MODELS OR FROM GW LABORATORY MEASUREMENTS

SSS range (pss)	0 to 38		33 to 36	
	STD	Mean	STD	Mean
GW2020 - GWlab				
ΔTb (K)	0.09	0.00	0.09	0.04
Δε'	0.10	0.00	0.10	0.04
Δε''	0.28	-0.00	0.26	-0.13
BV (α(T) adjustment) - GWlab				
ΔTb (K)	0.11	0.09	0.10	0.15
Δε'	0.50	-0.49	0.42	-0.65
Δε''	0.28	-0.00	0.27	-0.08
BVZ (α(T), τ(T) adjustments) - GWlab				
ΔTb (K)	0.10	-0.01	0.09	0.01
Δε'	0.18	0.02	0.11	-0.01
Δε''	0.28	0.01	0.26	-0.05
BVZ (α(T,S), τ(T) adjustments) - GWlab				

This article has been accepted for publication in IEEE Transactions on Geoscience and Remote Sensing. This is the author's version which has not been fully edited and content may change prior to final publication. Citation information: DOI 10.1109/TGRS.2023.3257923

> REPLACE THIS LINE WITH YOUR PAPER IDENTIFICATION NUMBER (DOUBLE-CLICK HERE TO EDIT) <   5

ΔTb (K)	0.09	-0.01	0.09	0.00
$\Delta\varepsilon'$	0.12	0.01	0.11	0.06
$\Delta\varepsilon''$	0.28	0.00	0.26	-0.05

C. New parametrization

Given the limitations described above, we investigate to which extent we can find an alternative parametrization that agrees with the new laboratory measurements and with the assumptions behind SoTr model.

When exploring an alternative parametrization of ε, ε_{BVZ} , we use the notations as in [6] (adjusted components are written in bold in the following equations):

$$\varepsilon_{BVZ} = \epsilon_1(T, S=0) +$$
$$\frac{\epsilon_S(T,S=0).(1-\boldsymbol{\alpha(T,S)}\cdot S) - \epsilon_1(T,S=0)}{1+j\nu/\boldsymbol{\nu1(T)}} - \frac{j\sigma(T,S)}{2\pi\epsilon_0\nu} \quad (4)$$

In this equation, ν is the radiation frequency, $\nu1$ is the first Debye relaxation frequency ($\omega\tau = \nu/\nu1$). We express $\nu1$ as a deviation from $\nu1$ fitted with laboratory freshwater measurements by [6], ν_{MW}, by introducing a function $g(T)$ as follows:

$$\nu_1(T) = \nu_{1MW}(T).(1 + g(T)) \quad (5)$$

We express α as:
$$\alpha(T,S) = f(T).(1 + h(S)) \quad (6)$$

The functional form of ε_{BV} is a particular case obtained with equations (4-6) in which $g(T) = h(S) = 0$

We explore a new parametrization, 'BVZ', based on laboratory measurements only, with the following constraints:

-1-The T,S dependency of the conductivity is prescribed by the PSS-78 relationship [15].

-2- Both α and ν1 parametrizations can be adjusted because GW laboratory measurements provide real and imaginary parts of ε.

-3- We consider that all S dependency is contained in σ and $\varepsilon_{s,}$ i.e. ν_1 is independent of S. A possible ν_1-S dependency will be discussed in section IV. We investigate two cases:

  a) $\varepsilon_{s,}$ varies linearly with S (hence fulfilling SoTr assumption): we adjust $g(T)$ and $f(T)$, $h(S) = 0$

  b) $\varepsilon_{s,}$ does not vary linearly with S: α depends on T and S and we adjust $g(T)$, $f(T)$ and $h(S)$.

-4-The number of fitted parameters has to respect the degrees of freedom of the system (the way we used to derive it is described in Annex 1).

We adjusted α and ν1 values using a two-step procedure described in annex 1. In order to minimize arbitrary choices concerning the functional form of fitted parametrizations, we first derived nonparametric functions using nonlinear generalized least squares approach[17]. Then, the functions are fitted to the adjusted values using polynomial relationships.

1) ε_{BVZ} derived with $\alpha(T)$, ν1(T) adjustments

The best adjustment to the GW laboratory measurements is found when α varies linearly with T and adjusted ν_1 is close to the $\nu_{1\,MW}$ (g(T)<0.04 for T<31°C, Figure 3).

$$f(T) = (f_0 - f_1 \cdot T) \quad (7)$$
$$g(T) = g_0 + g_1 \cdot T + g_2 \cdot T^2 \quad (8)$$

with:
$$\begin{bmatrix} f_0 \\ f_1 \end{bmatrix} = \begin{bmatrix} 0.002975810548577 \\ 0.000010686101917 \end{bmatrix}$$
and
$$\begin{bmatrix} g_0 \\ g_1 \\ g_2 \end{bmatrix} = \begin{bmatrix} 0.012693072655708 \\ -0.003428956751222 \\ 0.000132507806856 \end{bmatrix}$$
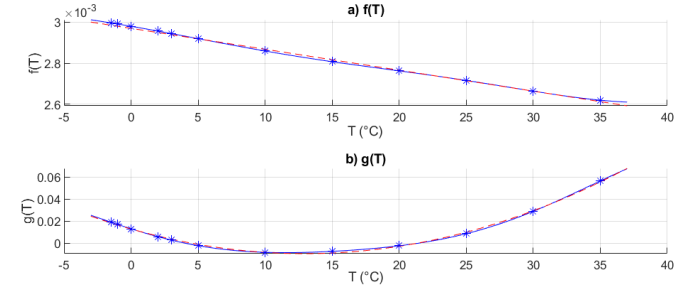

Figure 3: New parametrization of $\alpha(T)$ and $\nu_1(T)$. a) f(T) and b) g(T). Nonparametric functions are displayed in blue, blue stars indicate f(T) and g(T) values obtained for T conditions sampled in the laboratory. Polynomial fits of nonparametric functions are in dashed red.

As expected by construction, the residuals with respect to GW laboratory measurements (Figure 4) are lower than the residuals of BV with respect to GW laboratory measurements (Figure 2 c,d). STDD of ε' with respect to ε_{GWlab}' decreases from 0.48 to 0.18 and the mean difference between ε' and ε_{GWlab}' decreases from -0.44 to 0.02 (Table 2). However, ε' residuals appear to be systematically positive for SSS equal to 10 and 20 pss (Figure 4a). This motivates the addition of a salinity dependency on α.
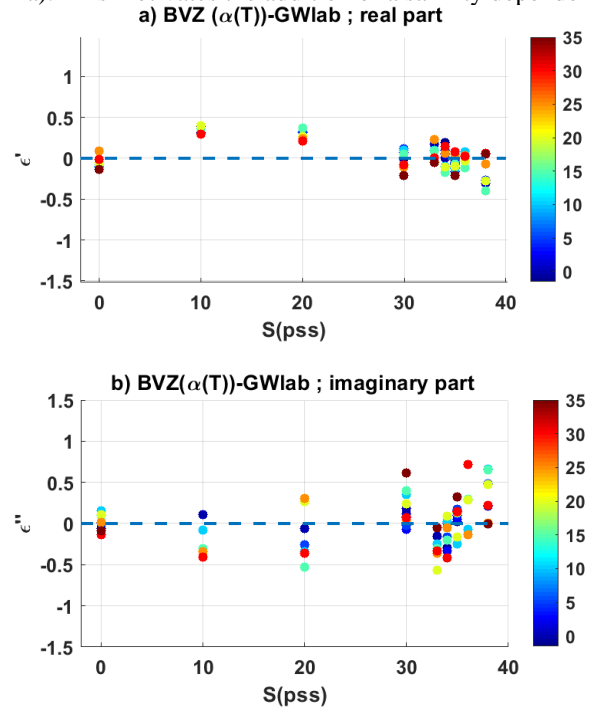

Figure 4: Difference between ε_{BVZ} estimated with new parametrization of $\alpha(T)$ and $\tau(T)$, and ε_{GWlab}: a) real part and b) imaginary part. Plots are functions of S (x axis) and T (°C, color bar). For each plot, mean difference and standard deviation of difference are reported in Table 2.

2) ε_{BVZ} derived from α(T,S), ν1(T) adjustments:

Following the formalism of equations (5) and (6), the corresponding parametrizations are:

$$f(T) = (f_{00} - f_{11} \cdot T) \quad (9)$$
$$h(S) = h_0 + h_1 \cdot S + h_2 \cdot S^2 + h_3 \cdot S^3 , \quad (10)$$
$$g(T) = g_{00} + g_{11} \cdot T + g_{22} \cdot T^2 \quad (11)$$

with

$$\begin{bmatrix} f_{00} \\ f_{11} \end{bmatrix} = \begin{bmatrix} 0.003100950226871 \\ 0.000010994028738 \end{bmatrix},$$

$$\begin{bmatrix} h_0 \\ h_1 \\ h_2 \\ h_3 \end{bmatrix} = \begin{bmatrix} 0.013179577518089 \\ 0.010461893723666 \\ -0.000744492408123 \\ 0.000011254875895 \end{bmatrix}, \text{ and}$$

$$\begin{bmatrix} g_{00} \\ g_{11} \\ g_{22} \end{bmatrix} = \begin{bmatrix} 0.012975352323248 \\ -0.003388740176732 \\ 0.000131313421124 \end{bmatrix}$$

Adding the dependency of α on S almost does not change the slope of f(T), nor the shape of g(T) (Figure 3 and Figure 5). The α dependency on S reaches 0.05 at 10°C and it is about -0.05 above 30pss (h function on Figure 5). This α(T,S) parametrization allows for the reduction of the STDD of ε_{BVZ}' with respect to ε_{GWlab}' from 0.18 to 0.12 with little change on ε_{BVZ}'' (TABLE 2) as it removes the systematic difference of ε_{BVZ}' at 10 and 20pss observed with α(T) parametrization.
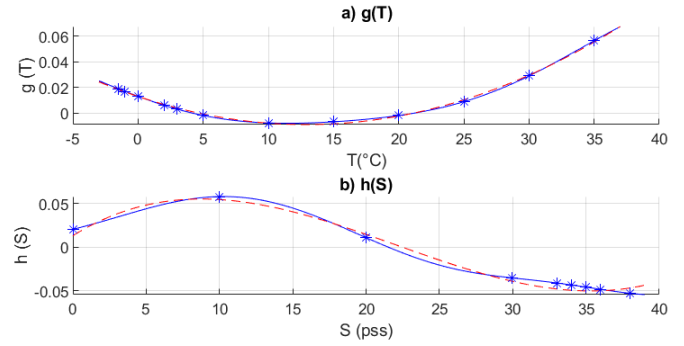

Figure 5: New parametrization of α(T,S) and τ(T). a) g(T), b) h(S). Nonparametric functions are displayed in blue, red stars indicate h(S) and g(T) values obtained for T and S conditions sampled in the laboratory. Polynomial fits to nonparametric functions are in dashed red,.

Compared to Tb simulated with GW2020 parametrization, Tb simulated with BVZ parametrization is in closer agreement with Tb derived from GW laboratory measurements between 33 and 36pss, as shown by the mean biases in Table 2. A better agreement appears especially in warm (>22°C) and fresh (<34) waters (blue background and blue dots on Figure 7).
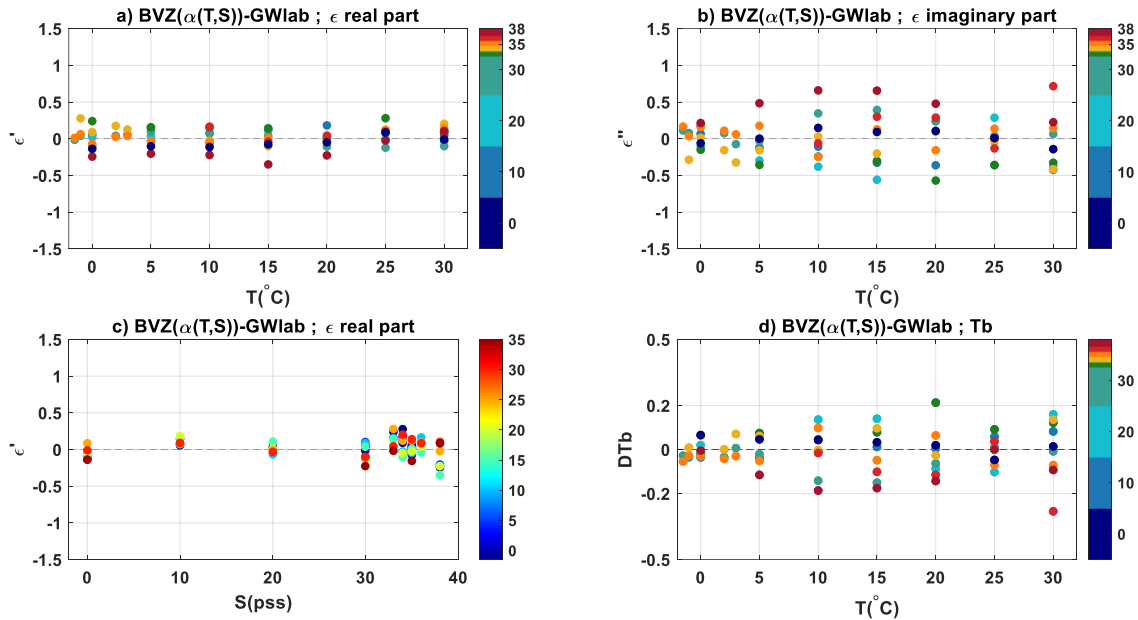

Figure 6: Difference between ε_{BVZ} estimated with new parametrization of α(T,S) and τ(T), and ε_{GWlab}: a,c) real part, as functions of T (x axis in a) and color scale in c)) and S (color scale in a) and x axis in c)), b)imaginary part, d) Difference in Tb at nadir between Tb_{BVZ} and Tb_{GWlab}. For each plot, mean difference and standard deviation of difference are given in Table 2.
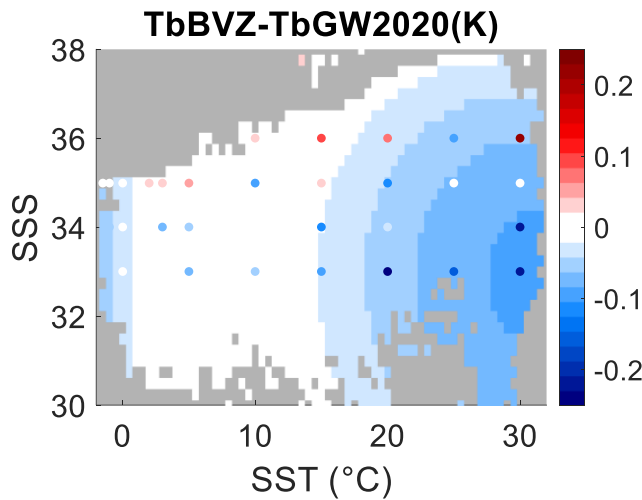
Figure 7: Differences in Tb at nadir simulated using BVZ and GW2020 dielectric constant models in the (SST,SSS) plane. The differences are plotted for SSS and SST commonly observed in the open ocean (70°N-70°S) as in Figure 1. The colored dots depict the difference between Tb derived from GW laboratory measurements and Tb simulated with GW2020 parametrization.

III. IMPACT OF THE NEW DIELECTRIC CONSTANT PARAMETRIZATION ON THE SMOS RETRIEVED SALINITY

A. Methodology

1) SMOS processing

The principle of SMOS SSS retrieval is described in [9]. We carried out an ensemble of 3 experiments corresponding to the 3 dielectric constant models BV, GW2020 and BVZ that we evaluate. Level-2 SSS is computed using SMOS Level-1 v724 Tb as primary input, and the SMOS Level-2 v700 processor [18] in which the various dielectric constant models are implemented and alternatively selected for the experiments. The tests are conducted during 4 months in a year, March, May, August, and November 2018, solely over descending orbits to reduce the effect of the ice-sea contamination. Only SSS retrieved at least 1000 km off the coast are considered, to minimize land-sea contamination in the test results. Level-3 SSS monthly fields are built from Level-2 SSS data retrieved through each dielectric constant model using the so-called validation protocol filtering (VPF). VPF consists of a set of constraints for rejecting Level-2 SSS data in accordance with control and science flags that are additional output of the Level-2 SMOS processor and that correspond to specific data quality criteria. VPF is summarized in Annex 2.

Processing SMOS data is quite computationally expensive, and hence, SSS retrievals from SMOS Level-1 v724 Tb were not performed using KS and MW dielectric constant models. Instead, we present in Annex 3 simplified estimates of the expected SSS differences when using those dielectric constant models.

2) Comparison with in situ near surface salinity

To evaluate the output from the 3 SMOS processing experiments introduced in the previous section, we use as in-situ reference the upper ocean measurements collected from Argo floats over the global ocean. Argo salinity values at 5m depth are considered. We consider only measurements retained by the quality controlled procedure of the In Situ Analysis System (ISAS) in which delayed mode profiles are used as much as possible and extra visual check is carried out [19, 20]. The evaluation of the monthly SSS with respect to Argo data at each valid grid bin (or "pixel") consists in comparing the statistics of SSS difference, computed spatially for each month, between the 3 SMOS experiments and Argo salinities. The statistics metrics that are used in the following are the median and the standard deviation (std), accompanied by their corresponding 95% confidence intervals calculated using bootstrapping [21].

B. Results

1) Systematic differences between parametrizations

The SSS differences between the different parametrization output products are the strongest in low SST regions below 10 or 5°C, as seen in Figure 8 for May 2018, and in Figure 9 for the 4 months altogether.

In tropical regions, GW2020 SSS is slightly larger than BV SSS, while BVZ SSS is slightly smaller. In high-latitudes, both GW2020 and BVZ SSS are smaller than BV, whereas in mid-latitudes BVZ is slightly saltier than BV. BVZ induces much saltier water than GW2020 in mid- and high-latitude regions ($\Delta SSS \geq 0.1$ pss), while BVZ is less salty than GW2020 in the tropical areas ($\Delta SSS \leq 0.08$ pss). Near the ice (around 0°C), GW2020 and BVZ yield similar SSS values while BV is much saltier ($\Delta SSS \geq 0.5$ pss).
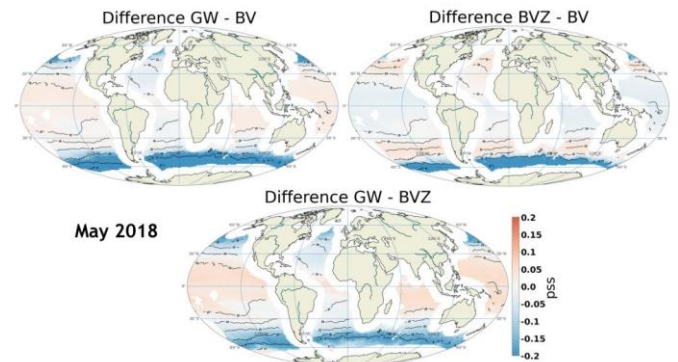

Figure 8: Global monthly difference maps obtained using the L3 SMOS SSS data during May 2018. (Top-Left) Difference between the GW2020 and BV parametrization, (Top-Right) Difference between the BVZ and BV parametrization, and (Bottom) Difference between the GW2020 and BVZ parametrization. Displayed value range is restricted between -0.2 pss and +0.2 pss to better highlight the differences. ECMWF SST isolines (black) are superimposed.

When considering the KS or MW dielectric constant models instead of BVZ, the SSS differences relative to those retrieved with BVZ oscillate more with SST, than the differences calculated with the SSS retrieved with the BV or GW models. With MW, differences of 0.1 and -0.12pss appear at 25°C and 10°C respectively. With KS, differences remain within +/- 0.03pss between 7 and 27°C, but exceed -0.7pss below 2°C (figure A3 in Appendix 3).
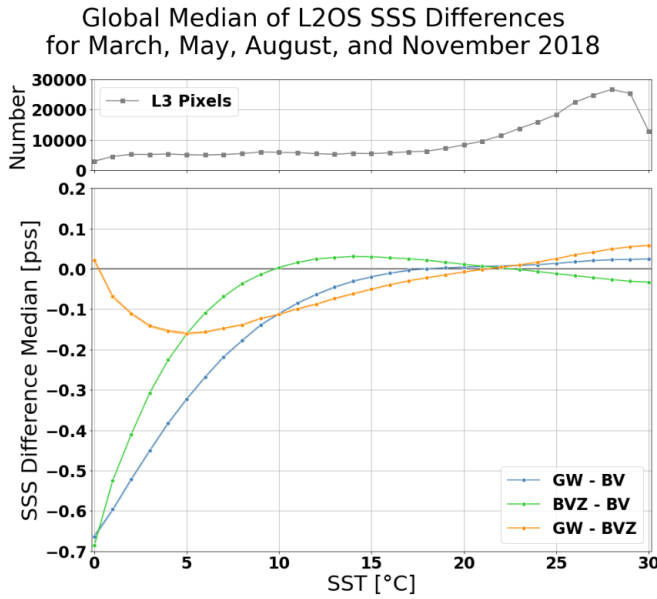
Figure 9: Comparison between the monthly L3 SMOS SSS yielded by the 3 dielectric constant parametrizations BV, GW2020 and BVZ. Comparison is shown for all 4 calculated months, March, May, August, and November 2018, and with respect to SST within the global ocean. (Top) Number of L3 pixels available for comparison within each 1°C bin. (Bottom) Median of pixelwise differences between the L3 SMOS SSS data within 1°C SST bins from -0.5°C to 30.5°C.

2)   Comparison with Argo

Overall, the global L3 processing and the worldwide distribution of 5m-depth Argo data permits calculation of SMOS-Argo salinity differences for 23,663 pixels during the 4-month period.

Differences between the SMOS L2 SSS and Argo SSS are relatively noisy over the global domain (Figure 10). The positive differences in the equatorial Pacific observed with the three parametrizations likely comes from an imperfect correction of roughness in presence of strong currents. Since this effect is very unlikely related to a dielectric constant issue, in the following we remove comparisons in the equatorial Pacific region (5°N-5°S). Sampling mismatch of the 5m-depth Argo dataset with respect to the satellite products is another uncertainty source for the comparison [22], which is not considered here. However, clear trends can be found over the domain and as functions of SST for the 4 calculated months (Figure 11). In warm waters (SST≥28°C, warm-pool regions), median biases (MB) with respect to Argo are limited to within ±0.05 pss for the 3 parametrizations. Between 27°C and 17°C, all 3 parametrizations yield a small positive MB (ΔSSS≤0.05 pss). From 17°C to around 10°C, BV and BVZ maintain relatively low SSS deviation from Argo (|ΔSSS|≤0.05 pss), while GW2020 MB is increasingly negative (ΔSSS<-0.1 pss). In colder waters down to about 2°C (high latitudes), MB yielded by the 3 parametrizations strongly diverge from each other: BV MB increases to more than +0.3 pss, GW2020 MB remains negative (between -0.1 and -0.2 pss), while BVZ MB stays limited to within ±0.05 pss. For waters colder than 2°C (polar ocean), both GW2020 and BVZ induce negative MB (ΔSSS<-0.15 pss), while BV MB is strongly positive (>0.35 pss).
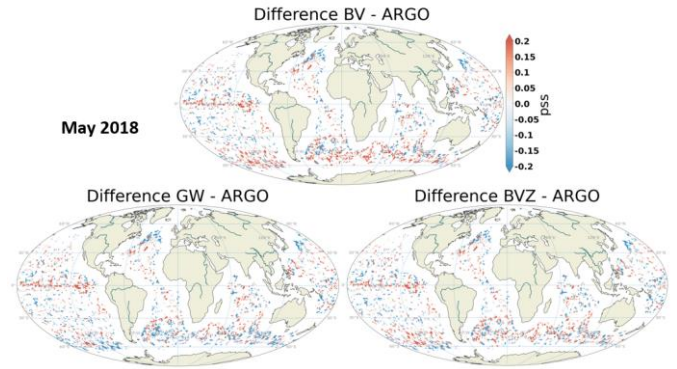

Figure 10: Global monthly difference maps for May 2018 between the three L3 SMOS experiment datasets and the 5m-depth Argo data. (Top) Salinity difference between BV parametrization output and Argo, (Bottom-Left) between GW2020 parametrization and Argo, (Bottom-Right) between BVZ parametrization and Argo. Displayed value range is restricted between -0.2 pss and +0.2 pss to better highlight the differences.

Standard deviations of difference (STDD) for the three parametrizations (not shown) are very similar across the entire SST range. Lowest STDD is found for SST>15°C (0.2-0.35 pss), while STDD becomes increasingly large when SST goes down to 0°C (0.4-0.65 pss).
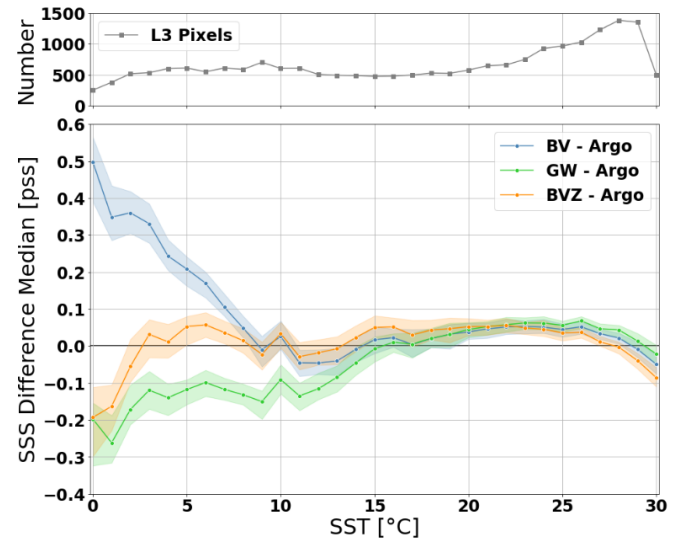

Figure 11: Comparison between the monthly L3 SMOS SSS (see text) for the 3 dielectric constant parametrizations BV, GW2020 and BVZ, and the 5m-depth Argo data. Comparison is shown for all 4 calculated months, March, May, August, and November 2018, and as a function of SST within the global ocean. Only L3 pixels at least 1000 km off the coastline are considered. (Top) Number of L3 pixels available for comparison within each 1°C bin. (Bottom) Median of pixelwise difference between L3 SMOS and mean Argo data within 1°C SST bins from -0.5°C to 30.5°C. 95% confidence intervals are displayed (shaded color) and were calculated using bootstrapping. Equatorial (within 5° latitude from the equator) Pacific SSS are not included as they are possibly wrongly affected by strong equatorial currents.

When considering the calculated months separately (see supplementary material), the MBs as functions of SST substantially vary from month to month and with respect to the

all-month set. Some of the 4 monthly periods show larger or smaller bias between the various parameterizations. The results for March and May 2018 are the closest to the all-month results. However, in August 2018 BV MB is the smallest on average among the 3 parametrizations, while in November 2018, GW2020 MB is the smallest for cold SST.

IV. DISCUSSION AND CONCLUSION

On the one hand, the advent of L-band radiometric satellite data, and on the other hand, new laboratory measurements of dielectric constant led to two separate revisions of the dielectric constant models used for the salinity retrieval from L-band radiometric measurements. Although the revised models, BV and GW2020, were derived using independent information, the relative variations of Tb estimated with both models are in remarkable agreement.

Still, each model has flaws. For BV, only α(T) was fitted to a degree-3 polynomial (yielding a near-parabolic function in T), and this simple adjustment was found to be insufficient to characterize ϵ_{GWlab} real and imaginary parts. This is consistent with the fact that radiometric measurements do not allow the derivation of the real and imaginary parts of the dielectric constant. For GW2020, the adjustment of as many as 21 coefficients using laboratory measurements that sample a limited range of oceanic temperature and salinity conditions can be questioned. In particular, in GW2020 the sea water conductivity was adjusted as a free parameter while the seawater samples used in the laboratory were calibrated with the PSS78 salinity-conductivity relationship. This led us to build a revised dielectric constant model, BVZ, by using the laboratory measurements and by limiting the number of adjusted parameters to 9. By adjusting these 9 parameters, we find residuals (0.12 and 0.28 for ϵ_{BVZ}' and ϵ_{BVZ}" respectively, TABLE 2) on the same order of magnitude as those obtained with GW2020 model, and of comparable order of magnitude as the uncertainties of GW laboratory measurements[8].

In order to model ϵ_{GWlab} dependency with respect to temperature, we find necessary to implement some linear temperature-dependency of α, and to increase ν1 from [6] both for cold temperatures (by ~2% at 0°C) and warm temperatures (by 3% at 30°C and 4 to 6% at 35°C; see the g(T) functions in Figure 3 and in Figure 5). This increase of the first Debye relaxation frequency of pure water renders it closer to [5] value as shown on Figure 4 of [6]. However, the linear variation of ϵ_s with S as assumed by SoTr does not permit a proper fit of ϵ_{GWlab} at 10pss and 20pss. This is resolved by adding a S dependency in α(S,T). Ellison et al. [23] argue that both ϵ_s and τ should vary linearly with S. We tested this hypothesis but adding a linear dependency of τ with respect to S did not improve the matching with ϵ_{GWlab}. In particular, the residuals at 10pss and 20pss remained very similar to the ones obtained with the α(T) and ν1(T) adjustment. We also tested some non-linear dependency of τ on S instead of a non-linear dependency of ϵ_s on S. However again, this did not yield a better ε fit while the non-parametric function was fluctuating much more than h(S). Distinguishing the influence of S on ϵ_s and τ could require the combination of measurements performed at various frequencies which was out of the scope of this study. On the other hand,

more laboratory measurements at S less than 30pss (e.g. measurements at 5, 15 and 25pss), and at S larger than 38pss (e.g. at 40pss), would result in better constraints on the adjustment shape at extreme S values. This is all the more important as very fresh salinity is often observed in strong variability regions, such as river plumes where the validation of satellite measurements using in situ point(wise) measurements is challenging. This is also important for salinity characterization in semi-enclosed seas such as the Baltic and Black Seas where salinity is less than 10 and 20 pss respectively or the Mediterranean Sea where SSS could reach 40 pss, especially in the context of a warming climate. Theoretical developments to explain the observed (S, T) dependency would also be very helpful to improve the parametrization.

SMOS SSS that is retrieved using the GW2020 and BVZ parametrizations is less biased in cold waters than SSS retrieved using BV (Figure 11). The different SMOS data versions, the different time periods used to derive BV parametrization, the low number of co-located points in cold water, and the large SMOS SSS noise, are all possible causes of this BV issue.

In cold waters, SMOS SSS retrieved with BVZ parametrization is on average closer to Argo SSS than SMOS SSS retrieved with GW2020 parametrization. It would be interesting to conduct a similar study with Aquarius and SMAP data sets.

This study highlights the value of deriving models independently of satellite measurements. Moreover, a dielectric constant parametrization derived independently of satellite measurements provides a new constraint to improve other RTM models (e.g. roughness model).

ANNEX 1: STRATEGY TO DERIVE NEW PARAMETRIZATION

Equation 4 depends on several functions (f(T),g(T),h(S)) that need to be estimated from GW laboratory data. The laboratory data are sampled regularly in (S,T) space and we assume that they have sufficient coverage to constrain the parameters. In other words, we consider that the functions do not exhibit fluctuations at scales smaller than the sampling. As described in [11], these functions are classically parameterized as polynomials of various degrees. Here, we choose to estimate these functions in two steps.

A first non-parametric step allows to extract these functions without making any assumption on the type of associated function. In order to constrain the functions at any point of their support, we use a sufficiently large correlation distance (at least twice as large as the sampling) to obtain a sufficiently smoothed result. This smoothing allows the inversion to be more stable. It is partly controlled by the residuals.

A second step consists in estimating a parametrization associated with these functions in order to simplify their representation.

This two-step approach is effective because it allows to establish the variations of the various functions without making them fit into a too rigid parametric framework. It is only afterwards, in view of the non-parametric estimates, that the representation of these functions is simplified by using polynomials. Furthermore, the non-parametric approach allows us to calculate the expected number of degrees of freedom (DOFFS, see [24]), i.e. the number of independent constraints

that the data actually carry. In a non-parametric case, this number can be non-integer.

In order to estimate the functions, we take a Bayesian formalism as described in [17] and [24]. This type of approach involves the minimization of a quadratic cost function that incorporates a maximum likelihood term and a regularization term. This last term constitutes the a priori knowledge that we have on each function and is translated into covariances that act as smoothing operators.

The cost function is written:

$$C(p) = <(d-\varepsilon_{BVZ}(p))^T.(d-\varepsilon_{BVZ}(p))> + <((p-p_0)^T.C_p.(p-p_0))> \quad (12)$$

where d is the vector of GW observations, $p = \begin{pmatrix} f \\ h \\ g \end{pmatrix}$ and C_p is the covariance operator which combines the covariances of the functions (f,g,h) and p0 is the a priori function values.

C_p is written :

$$C_p = \begin{bmatrix} C_f & 0 & 0 \\ 0 & C_h & 0 \\ 0 & 0 & C_g \end{bmatrix}$$

with :

$$C_f(T,T') = \sigma_f^2 \exp\left(-\frac{(T-T')^2}{\xi_f^2}\right)$$

$$C_h(S,S') = \sigma_h^2 \exp\left(-\frac{(S-S')^2}{\xi_h^2}\right)$$

$$C_g(T,T') = \sigma_g^2 \exp\left(-\frac{(T-T')^2}{\xi_g^2}\right)$$

Correlation distances ξ_f, ξ_h and ξ_g are set to 20°C, 20pss and 20°C respectively. Different tests have been performed with different correlation lengths. With smaller correlation lengths, oscillations appear in the solution without improving the data fitting (the chi2 does not decrease significantly).

The a priori function vector is written as:

$$p_0 = \begin{pmatrix} f_0 \\ h_0 \\ g_0 \end{pmatrix}$$

A priori values are taken as :
-a constant value for f(T), equal to 0.00314 as suggested by [11].
- h(S)=g(T)=0 assuming that S does not depend on f and that $v1$ derived by [6] is correct. The latter assumption is because [6] used more laboratory measurements performed at various frequency than [16] to derive $v1$. However, the general shape of the functions is the same whatever [6] or [16] formulation (as used by [11]) is used. The a priori standard deviations σ_f, σ_g and σ_h are taken equal to 0.001, 0.2 and 0.4 respectively.

The goal is to find the value of $p = \tilde{p}$ that minimizes C(p).

$\varepsilon_{BVZ}(p)$ model is non-linear according to p. C(p) is performed iteratively using the Raphson-Newton method:

$$\tilde{p}_{k+1} = p_0 + C_p \cdot G_k^T \cdot H_k^{-1} \cdot (d - \varepsilon_{BVZ}(\tilde{p}_k)$$
$$+ G_k \cdot (\tilde{p}_k - p_0)) \quad (13)$$

G_k is the derivative of the direct model $\varepsilon_{BVZ}(\tilde{p}_k)$ according to p in $\tilde{p}_k$. Explicitly, it is the following operator:

$$G_k = \begin{bmatrix} \partial\varepsilon_{BVZ\_1}/\partial f & \partial\varepsilon_{BVZ\_1}/\partial h & \partial\varepsilon_{BVZ\_1}/\partial g \\ \vdots & \vdots & \vdots \\ \partial\varepsilon_{BVZ\_n}/\partial f & \partial\varepsilon_{BVZ\_n}/\partial h & \partial\varepsilon_{BVZ\_n}/\partial g \end{bmatrix}$$

where ε_{BVZ_i} is the model calculated at the point (S_i,T_i) of laboratory measurement i, i varying between 1 and n. The matrix has the dimension (n,3), n being the number of data. The Frechet derivatives $\partial\varepsilon_{BVZ}/\partial f$, $\partial\varepsilon_{BVZ}/\partial h$ et $\partial\varepsilon_{BVZ}/\partial g$ can be seen as functional operators as well as matrix operators [17].

$C_p \cdot G_k^T \cdot H_k^{-1}$ is the gain applied to the residual vector $d - \varepsilon_{BVZ}(\tilde{p}_k) + G_k(\tilde{p}_k - p_0)$ with $H_k = (I + G_k \cdot C_p \cdot G_k^T)$, where I is the unit matrix whose dimension is n $\times$ n.

We note V_k the vector $H_k^{-1} \cdot (d - \varepsilon_{BVZ}(\tilde{p}_k) + G_k(\tilde{p}_k - p_0))$. After convergence (k=10 ; indeed, the solution and the Chi2 stabilize after typically 4 iterations), we estimate the parameters $(\tilde{f}(T), \tilde{h}(S), \tilde{g}(T))$ using equation (13).

The approximation of the functions $(\tilde{f}(T), \tilde{h}(S), \tilde{g}(T))$ by polynomials is obtained using the polyfit function of matlab. The degree of the polynomials fitting (f,h,g) is 1, 3 and 2, respectively. This choice degrades the residuals in a non-significant way. Note that the number of fitted polynomial coefficients is 9 in the α(T,S) case. This is in line with the a posteriori DOFFS [24] calculated in the first step, which is equal to 9.1.

ANNEX 2: SMOS DATA PROCESSING

Level-2 SMOS SSS are filtered according to validation protocol flags (Table A1).

Monthly SSS fields are built on a grid composed of about 100 km x 100 km bins (see later) using a weighting average within one bin:

$$\langle SSS \rangle = \sum_{j=1}^{N} \frac{SSS_j}{R_j^2 \sigma_j^2} \times \left(\sum_{j=1}^{N} \frac{1}{R_j^2 \sigma_j^2}\right)^{-1}$$

where SSS_j is the jth Level-2 value within the bin, R_j the equivalent footprint diameter relative to the corresponding dwell-line, σ_j the theoretical error yielded by the Level-2 processor for that value, and N the number of measurements available within the bin. As we are treating Level-2 half-orbit (descending) data, the averaged $\langle SSS \rangle$ value is considered valid if $N \geq 30$. The grid is based on the Hierarchical Equal Area isoLatitude Pixelization of a sphere (HEALPix, https://healpix.jpl.nasa.gov/healpixBackgroundReferences.shtml), using a N_{side} parameter value of 64 for which each bin area is 10377.3 km² (49152 pixels over the entire Earth).

Table A1:
Quality-control and science flags used in VPF (1=True, 0=False).

Flag name	Meaning	VPF value
DG_AF_FOV	Number of measurements in alias-free Field of View	≥130
FG_CTRL_ECMWF	No missing ECMWF data	1
FG_CTRL_NUM_MEAS_MIN	Very few measurements	0
FG_CTRL_NUM_MEAS_LOW	Number of valid measurements below threshold (30)	0
FG_CTRL_MANY_OUTLIERS	Number of outliers above threshold	0
FG_CTRL_SUNGLINT	Number flagged for sun glint above threshold	0
FG_CTRL_MOONGLINT	Number flagged for moon glint above threshold	0
FG_CTRL_REACH_MAXITER	Number of iterations above threshold	0
FG_CTRL_MARQ	Minimization procedure factor above threshold	0
FG_CTRL_CHI2_P	χ^2 minimized value above threshold	0
FG_CTRL_SUSPECT_RFI	Number flagged for RFI above threshold	0
SC_LOW_WIND	Low wind speed	1
SC_LAND_SEA_COAST1	Not land and not near coast	1
SC_ICE	Ice present	0
SC_SUSPECT_ICE	Possible ice contamination	0

ANNEX 3: SIMPLIFIED ESTIMATE OF SSS DIFFERENCES

Since SMOS data processing is quite computationally expensive, we have derived a simplified way to estimate the SSS difference expected from the use of various dielectric constant models.

Let Tb$_{model1}$ and Tb$_{model2}$ be the Tb simulated under the same SSS and SST conditions with two different dielectric constant models, and ΔTb$_{model}$ their difference. The expected retrieved SSS difference, ΔSSS, is derived from the derivative of Tb with respect to SSS at the given (SSS,SST), after taking into account the change in Tb coming from the different OTT estimates when using two different models, ΔTb$_{OTT}$.

We approximate the retrieval of SMOS SSS from multiple Tb measured in full polarizations at incidence angle varying between nadir and ~60° by a retrieval from a nadir Tb, considering that for most SMOS incidence angles derivatives of nadir Tb and of Stokes 1 parameter are very similar and neglecting the adjustment of the wind speed made in the course

of SMOS SSS retrieval. Considering Figure 3 of [25] at nadir, we approximate the ΔSSS as:

$$\Delta SSS = \frac{\Delta Tb}{(0.015 \cdot SST + 0.25)}$$

With $\Delta Tb = \Delta Tb_{model} - \Delta Tb_{OTT}$.

ΔTb_{OTT} is an estimate of the mean difference of Tb derived over the OTT region with the two considered models at nadir. It is estimated for SST varying between 10°C and 25°C. The mean differences as function of SST (Figure A3) are weighted by the distribution of pixels over (SST, SSS) pairs commonly observed over the open ocean (FIGURE 1f). We validate this simplified approach by comparing ΔSSS such obtained with the GW-BV, BVZ-BV and GW-BVZ SSS differences obtained with full SMOS SSS retrievals (FIGURE 9). We observe very good consistency of the differences, with only few significant differences close to 0°C possibly due to artefacts of ice-sea contamination.
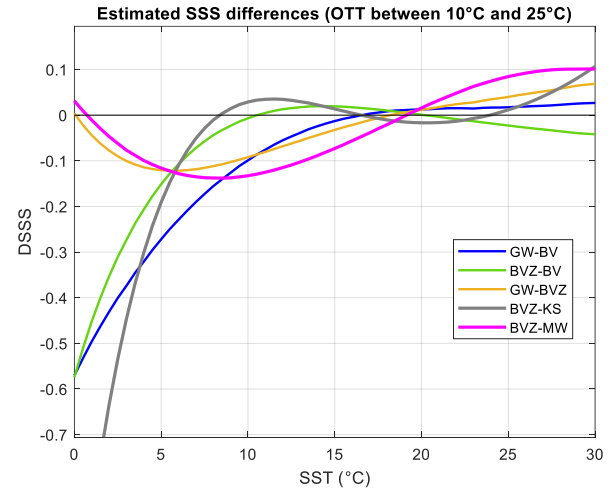

Figure A3: Simplified estimate of differences of SMOS SSS yielded by the 5 dielectric constant parametrizations BV, GW2020, KS, MW and BVZ as function of SST.

ACKNOWLEDGEMENTS

REFERENCES

[1]   J. Boutin et al., "Satellite-Based Sea Surface Salinity Designed for Ocean and Climate Studies," Journal of Geophysical Research: Oceans, vol. 126, no. 11, p. e2021JC017676, 2021, doi: https://doi.org/10.1029/2021JC017676.
[2]   N. Reul et al., "Sea surface salinity estimates from spaceborne L-band radiometers: An overview of the first decade of observation (2010–2019)," Remote Sensing of Environment, vol. 242, p. 111769, 2020/06/01/ 2020, doi: https://doi.org/10.1016/j.rse.2020.111769.
[3]   N. Vinogradova et al., "Satellite Salinity Observing System: Recent Discoveries and the Way Forward," (in English), Frontiers in Marine Science, Review vol. 6, no. 243, 2019-May-22 2019, doi: 10.3389/fmars.2019.00243.

This article has been accepted for publication in IEEE Transactions on Geoscience and Remote Sensing. This is the author's version which has not been fully edited and content may change prior to final publication. Citation information: DOI 10.1109/TGRS.2023.3257923

> REPLACE THIS LINE WITH YOUR PAPER IDENTIFICATION NUMBER (DOUBLE-CLICK HERE TO EDIT) <   12

[4]   D. M. L. Vine, R. H. Lang, Y. Zhou, E. P. Dinnat, and T. Meissner, "Status of the Dielectric Constant of Sea Water at L-Band for Remote Sensing of Salinity," *IEEE Transactions on Geoscience and Remote Sensing,* vol. 60, pp. 1-14, 2022, doi: 10.1109/TGRS.2022.3207944.

[5]   L. Klein and C. Swift, "An improved model for the dielectric constant of sea water at microwave frequencies," *IEEE Transactions on Antennas and Propagation,* vol. 25, no. 1, pp. 104-111, 1977.

[6]   T. Meissner and F. J. Wentz, "The complex dielectric constant of pure and sea water from microwave satellite observations," *IEEE Transactions on Geoscience and Remote Sensing,* vol. 42, no. 9, pp. 1836-1849, 2004.

[7]   T. Meissner and F. J. Wentz, "The Emissivity of the Ocean Surface Between 6 and 90 GHz Over a Large Range of Wind Speeds and Earth Incidence Angles," *IEEE Transactions on Geoscience and Remote Sensing,* vol. 50, no. 8, pp. 3004-3026, 2012.

[8]   Y. Zhou, R. H. Lang, E. P. Dinnat, and D. M. L. Vine, "Seawater Debye Model Function at L-Band and Its Impact on Salinity Retrieval From Aquarius Satellite Data," *IEEE Transactions on Geoscience and Remote Sensing,* pp. 1-14, 2021, doi: 10.1109/TGRS.2020.3045771.

[9]   J. Boutin *et al.*, "Correcting Sea Surface Temperature Spurious Effects in Salinity Retrieved From Spaceborne L-Band Radiometer Measurements," *IEEE Transactions on Geoscience and Remote Sensing,* vol. 59, no. 9, pp. 7256-7269, 2021, doi: 10.1109/tgrs.2020.3030488.

[10]   P. J. W. Debye, *Polar molecules*. New York: The Chemical Catalog Company, Inc. (in English), 1929.

[11]   R. Somaraju and J. Trumpf, "Frequency, Temperature and Salinity Variation of the Permittivity of Seawater," *IEEE Transactions on Antennas and Propagation,* vol. 54, no. 11, pp. 3441-3448, 2006.

[12]   R. Lang, Y. Zhou, C. Utku, and D. Le Vine, "Accurate measurements of the dielectric constant of seawater at L band," *Radio Science,* vol. 51, no. 1, pp. 2-24, 2016, doi: 10.1002/2015rs005776.

[13]   Y. Zhou, R. H. Lang, E. P. Dinnat, and D. M. L. Vine, "L-Band Model Function of the Dielectric Constant of Seawater," *IEEE Transactions on Geoscience and Remote Sensing,* vol. 55, no. 12, pp. 6964-6974, 2017.

[14]   P. Waldteufel, J. Vergely, and C. Cot, "A modified cardioid model for Processing multiangular radiometric observations," *IEEE Transactions on Geoscience and Remote Sensing,* vol. 42, no. 5, pp. 1059-1063, 2004.

[15]   IOC, SCOR, and IAPSO, "The international thermodynamic equation of seawater – 2010: Calculation and use of thermodynamic properties," Intergovernmental Oceanographic Commission, Manuals and Guides No. 56, UNESCO (English), 196 pp., 2010.

[16]   A. Stogryn, H. Bull, K. Rubayi, and S. Iravanvhy, "The microwave dielectric properties of sea and fresh water," GenCorp, Aerojet, Azusa, Ca. 91702, 1995.

[17]   A. Tarantola and B. Valette, "Generalized nonlinear inverse problems solved using the least squares criterion," *Reviews of Geophysics,* vol. 20, no. 2, pp. 219-232, 1982, doi: https://doi.org/10.1029/RG020i002p00219.

[18]   N. Reul *et al.*, "SMOS L2 OS Algorithm Theoretical Baseline Document ", SO-TN-ARG-GS-0007, 21 February 2021 2021. [Online]. Available: https://earth.esa.int/eogateway/documents/20142/37627/SMOS-L2OS-ATBD.pdf

[19]   F. Gaillard, T. Reynaud, V. Thierry, N. Kolodziejczyk, and K. v. Schuckmann, "In Situ–Based Reanalysis of the Global Ocean Temperature and Salinity with ISAS: Variability of the Heat Content and Steric Height," *Journal of Climate,* vol. 29, no. 4, pp. 1305-1323, 2016, doi: 10.1175/jcli-d-15-0028.1.

[20]   N. Kolodziejczyk, A. Prigent-Mazella, and F. Gaillard, "ISAS temperature and salinity gridded fields," 2021, doi: https://doi.org/10.17882/52367.

[21]   B. Efron, "Nonparametric estimates of standard error: The jackknife, the bootstrap and other methods," *Biometrika,* vol. 68, no. 3, pp. 589-599, 1981, doi: 10.1093/biomet/68.3.589.

[22]   C. Thouvenin-Masson *et al.*, "Satellite and In Situ Sampling Mismatches: Consequences for the Estimation of Satellite Sea Surface Salinity Uncertainties," *Remote Sensing,* vol. 14(8):1878, 2022, doi: https://doi.org/10.3390/rs14081878

[23]   W. Ellison *et al.*, "New permittivity measurements of seawater," *Radio Science,* vol. 33, no. 3, pp. 639-648, 1998.

[24]   C. D. Rodgers, *Inverse methods for atmospheric sounding : theory and practice*. Singapore ; [River Edge, N.J.] : World Scientific, 2000.

[25]   S. H. Yueh, R. West, W. J. Wilson, F. K. Li, E. G. Njoku, and Y. Rahmat-Samii, "Error sources and feasibility for microwave remote sensing of ocean surface salinity," *IEEE Transactions on Geoscience and Remote Sensing,* vol. 39, no. 5, pp. 1049-1060, 2001.

Jacqueline Boutin received the Ph.D. degree in physical methods in remote sensing from the University Paris VII, Paris, France, in 1990. She is Senior Research Scientist at the Centre National de la Recherche Scientifique (CNRS), deputy director of the Laboratoire d'Océanographie et du Climat-Expérimentation et Approches Numériques (LOCEAN), Paris, France. She has widely studied the validity of remotely-sensed wind speeds and the ocean-atmosphere exchange of CO_2 at large scale using both satellite (wind speeds, sea surface temperature, and ocean color) and *in situ* data (in particular, carbon-interface ocean-atmosphere autonomous drifters, CARIOCA). Since 1999, she is involved in the Soil Moisture and Ocean Salinity mission. She participated in the development of an L-band sea surface emissivity model and in several airborne campaigns (WISE and EuroSTARRS). She coordinates the scientific activities of the French SMOS-Ocean team, of the European Space Agency (ESA) Climate Change Initiative Sea Surface Salinity project and she participates to the ESA Expert Support Laboratories that define and validate the processing of SMOS Level 2 measurements for the retrieval of Sea Surface Salinity.

Jean-Luc Vergely received the engineering degree from the Ecole Nationale du Génie des Eaux et de l'Environnement de Strasbourg, Strasbourg, France, in 1988, and the Ph.D. degree in statistics applied to astronomy from Louis Pasteur University, Strasbourg, France, in 1998. He has been responsible for managing cooperative projects in Africa. Since 2002, he is senior research engineer in ACRI-ST company, France.

Fabrice Bonjean obtained his doctorate in Oceanography, Meteorology and Environment at the Pierre and Marie Curie University (Paris 6) in 1998. He participated for 9 years in the USA in NASA and NOAA projects related to ocean currents. He has worked in the private sector on topics related to ocean and weather conditions in support of offshore engineering and in particular the design of renewable energy production units around the world. He is currently a researcher under contract with the CNRS at the LOCEAN laboratory in Paris, France.

Yiwen Zhou (Member, IEEE) received the B.S. degree in electrical engineering from Southeast University, Nanjing, China, in 2010, and the M.S. and Ph.D. degrees in electrical engineering from The George Washington University (GWU), Washington, DC, USA, in 2012 and 2017, respectively. He then did post-doctoral work at GWU for modeling radar backscatter from vegetation canopy and the impact of seawater dielectric model on ocean salinity retrieval. He was a Research Scientist with Lincoln Agritech Ltd., Lincoln University, Christchurch, New Zealand. Presently, he is a Scientist with Swiss Federal Institute for Forest, Snow and Landscape Research (WSL), Birmensdorf, Zürich, Switzerland. He is a member of IEEE GRSS and a senior member of URSI. His research interests include, microwave dielectric measurements and sensor design, scattering model development and remote sensing of ocean salinity, soil moisture and vegetation dynamics.

Emmanuel P. Dinnat (M'12–SM'16) received an advanced studies degree in instrumental methods in astrophysics and spatial applications and the Ph.D. degree in computer science, telecommunications, and electronics from University Pierre and Marie Curie, Paris, France, in 1999 and 2003, respectively. He is currently a Research Scientist with the Cryospheric Sciences Laboratory, NASA Goddard Space Flight Center, Greenbelt, MD, USA. He is working on the calibration and validation and algorithm improvements for the Soil Moisture and Ocean Salinity, the Aquarius/SAC-D, and the Soil Moisture Active Passive missions. His latest research focuses on high latitude oceanography and the interactions between the cryosphere and oceans. His research interests include active and passive microwave remote sensing, sea surface salinity, scattering from rough surfaces, atmospheric radiative transfer, and numerical simulations.